A Control Architecture of a Distributed Actuator System for a Bio-Inspired Spine

Bonhyun Ku and Arijit Banerjee

***Abstract*—Control of an articulated spine is important for humanoids' dynamic and balanced motion. Although there have been many spinal structures for humanoids, their actuation is still limited due to the usage of geared-motors for joints. This paper introduces position control of a distributed electromechanical spine in a vertical plane. The spine dynamics model is approximated as an open chain. Gravitational and spring torques are compensated for the control. Moreover, torque-to-current conversion for the actuator is developed. Experimental results show the implemented control of the electromechanical spine for undulatory motions.**

I. Introduction

The spine and surrounding muscles make vertebrates flexible, dynamic, balanced, and natural [1]–[4]. For example, a cheetah's ability to efficiently gallop has been attributed to its elastic spine [5]. Humans also use their spine extensively for energy-efficient locomotion and balance by actively controlling the center-of-mass [6]. Bio-inspired robots have often been envisioned to include an artificial spine. For example, a differential actuated spine was contemplated for MIT Cheetah [7]. Similarly, humanoids such as "Kojiro", "Kenshiro", and "Kengoro" [8]–[10] used spine structures created using tendon-driven motors. Adding distributed springs within these articulated spines further improved the supporting force [11]. Conventionally, a motor-driven actuator has been one of the most preferred approaches to create articulated spines [12]–[14].

Instead of tendon-driven joint actuation with motors and gears, an alternative gearless, bio-inspired electromechanical actuation system for a spine was introduced in [15]. This modular and distributed actuator combines the spine structure along with its actuation mechanism, as shown in Fig. 1. Each module consists of an E-shaped core and two coils. The E-shaped core resembles a vertebra and two coils emulate the surrounding muscles. The two coils in the module produce antagonistic torques, an actuating principle found in abundance in biological systems. Integration of mechanical springs between two adjacent modules further improves the actuator's torque capability along with its ability to store mechanical energy [16]. A system-level design methodology for the distributed spine showed that the spine can produce a total of 113.4 Nm torque while having a size that can fit in a humanoid such as "THORMANG 3" [17]. One of the remaining questions in this pursuit is—how can we control such a bio-inspired, distributed actuation system to achieve a desired trajectory? Unlike conventional motors, the proposed distributed actuator's torque characteristic is a highly nonlinear function of position and coil current. The nonlinearity gets further amplified due to the magnetic core saturation and airgap fringing effect [18]. A dynamic model of the spine and the actuator's precise torque-to-current conversion are necessary to create the control framework. Additionally, closed-loop control with gravity compensation is needed to operate the spine in a vertical plane with smooth transient behavior [19], [20].

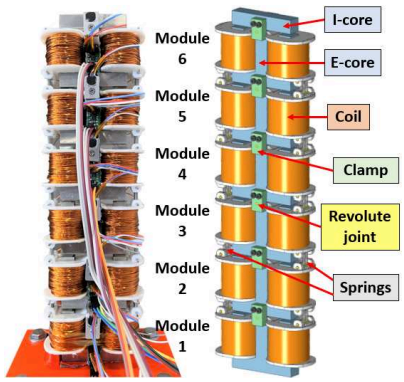

Fig. 1: The vertical electromechanical spine with distributed springs.

This paper presents the spine dynamics and closed-loop position control of the electromechanical spine with distributed springs in a vertical plane. The position controller includes PD control with on-line gravity and spring torque compensations. The actuator's torque-to-current conversion gain is calculated using a finite-element based simulation to account for the non-linearity. Stiffer springs are utilized in lower modules to offset higher torque requirement while operating in a vertical plane. Different combinations of linear extension springs are utilized at each joint. The distributed springs create a vertical equilibrium position for the spine. This approach minimizes the input energy needed to keep the spine vertically straight. Experimental results using the prototype built in [15] show that the proposed actuator can be controlled to achieve undulatory motions at 1 Hz for a swing of 18 deg, from Joint 1 to Joint 6.

Section II presents the actuator's module operation, spine dynamics model approximation, torque-to-current conversion, spine controller architecture, and distributed springs. Simulation results for swing and phase-shifted motions of the electromechanical spine are presented in Section III and compared to its analytical model. Experimental results with closed-loop control are provided in Section IV.

Department of Electrical and Computer Engineering, University of Illinois at Urbana-Champaign, Urbana, IL, USA [bonhyun2, arijit]@illinois.edu

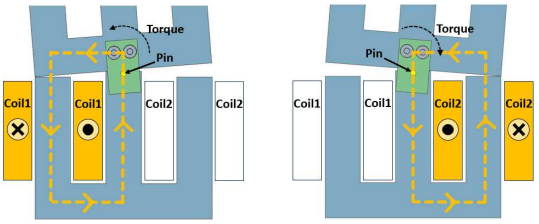

(a) (b)

Fig. 2: A single module rotates by selective excitation: (a) The upper module rotates counter-clockwise when Coil 1 is excited. (b) The upper module rotates clockwise when Coil 2 is excited.

II. Vertical Electromechanical Spine with Springs

A. Actuation Principle

Adjacent modules work together to produce torque, as shown in Fig. 2. The dashed line shows the magnetic flux path when a coil is excited. When Coil 1 is excited, the upper module rotates counter-clockwise, and when Coil 2 is excited, it rotates clockwise with the pin being the axis of rotation. Each joint allows ± 4.5 deg from the straightened position. Analytical model, module design procedure, mechanical designs, multi-module operation, and force measurements of the actuator were analyzed in [15].

B. Spine Dynamics

The electromechanical spine structure is a 6-link planar open chain, as shown in Fig. 3. Only two joints are shown, because all of the modules are identical. Since module 6 only moves a small I-core, joint 6 is ignored for model simplicity. The 5-link spine dynamics can be written as

$$\tau = M(\theta)\ddot{\theta} + c(\theta, \dot{\theta}) + g(\theta), \tag{1}$$

where angular positions $\theta = [\theta_1,\ \theta_2,\ \theta_3,\ \theta_4,\ \theta_5]^T$, mass matrix $M(\theta)$, Coriolis and centripetal torque $c(\theta, \dot{\theta})$, and the gravitational torque $g(\theta)$ [21]. The spine's zero configuration is $\theta = [\frac{\pi}{2},\ 0,\ 0,\ 0,\ 0]^T$ for vertically straight positions. Unlike common multi-link open chain with motors at joints,

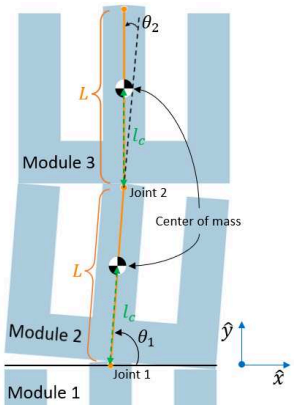

Fig. 3: The spine structure is 6-link planar open chain with limited angular flexibility.

the distributed spine has a small angular flexibility at each joint. Since each joint has only ± 4.5 deg position range, $\theta \approx [\frac{\pi}{2},\ 0,\ 0,\ 0,\ 0]^T$ can be used to approximate $M(\theta)$ as a constant matrix M. Moreover, considering low angular velocities, $c(\theta, \dot{\theta})$ becomes negligible. Therefore, the dynamics of the electromechanical spine becomes

$$\tau = M\ddot{\theta} + g(\theta). \tag{2}$$

The module's rotational inertia matrix is obtained from Creo CAD software. Using this rotational inertia matrix, the mass matrix M is analytically computed at zero configuration and is given by

$$M = \begin{bmatrix} 0.0236 & 0.0167 & 0.0104 & 0.0051 & 0.0015 \\ 0.0167 & 0.0123 & 0.0079 & 0.0040 & 0.0012 \\ 0.0104 & 0.0079 & 0.0054 & 0.0029 & 0.0009 \\ 0.0051 & 0.0040 & 0.0029 & 0.0018 & 0.0006 \\ 0.0015 & 0.0012 & 0.0009 & 0.0006 & 0.0003 \end{bmatrix}. \tag{3}$$

The relative error between the mass matrix at zero configuration and fully-rotated positions (all joints rotated by 4.5 deg) is negligible as shown below:

$$M_{RE} = \begin{bmatrix} 0.75 & 0.71 & 0.87 & 1.24 & 1.80 \\ 0.71 & 0.48 & 0.46 & 0.65 & 1.05 \\ 0.87 & 0.46 & 0.26 & 0.27 & 0.50 \\ 1.24 & 0.65 & 0.27 & 0.10 & 0.15 \\ 1.80 & 1.05 & 0.50 & 0.15 & 0.00 \end{bmatrix} \%. \tag{4}$$

Gravitational torque $g(\theta)$ is calculated with the Lagrangian formulation using point mass of a module, expressed as

$$g(\theta) = mg \begin{bmatrix} \sigma_5 + \sigma_4 + \sigma_3 + \sigma_2 + \sigma_1 \\ \sigma_4 + \sigma_3 + \sigma_2 + \sigma_1 \\ \sigma_3 + \sigma_2 + \sigma_1 \\ \sigma_2 + \sigma_1 \\ \sigma_1 \end{bmatrix},$$

$$\begin{aligned} \text{where } \sigma_1 &= l_c \cos(\theta_1 + \theta_2 + \theta_3 + \theta_4 + \theta_5), \\ \sigma_2 &= (L + l_c) \cos(\theta_1 + \theta_2 + \theta_3 + \theta_4), \\ \sigma_3 &= (2L + l_c) \cos(\theta_1 + \theta_2 + \theta_3), \\ \sigma_4 &= (3L + l_c) \cos(\theta_1 + \theta_2), \\ \sigma_5 &= (4L + l_c) \cos\theta_1. \end{aligned} \tag{5}$$

L is the link length, l_c is the center-of-mass distance from joint, and m is the mass of a single module, which are described in Fig. 3.

The spine dynamics model (2) and its approximated M and $g(\theta)$ are used to calculate torque for the trajectories. L = 42mm, l_c = 22.08mm, and m = 0.31kg are used for the model parameters. The spine dynamics is plotted in Fig. 4(a) and 4(b) for its sinusoidal swing and phase-shifted motions. Note that joint position changes from its zero configuration are plotted in degrees. For the swing motion as shown in Fig. 4(a), all joint position references are in phase, resulting in sinusoidal joint torques in phase with different magnitudes. The torque at Joint 1 is the highest, since it has the longest moment arm. The magnitude of the

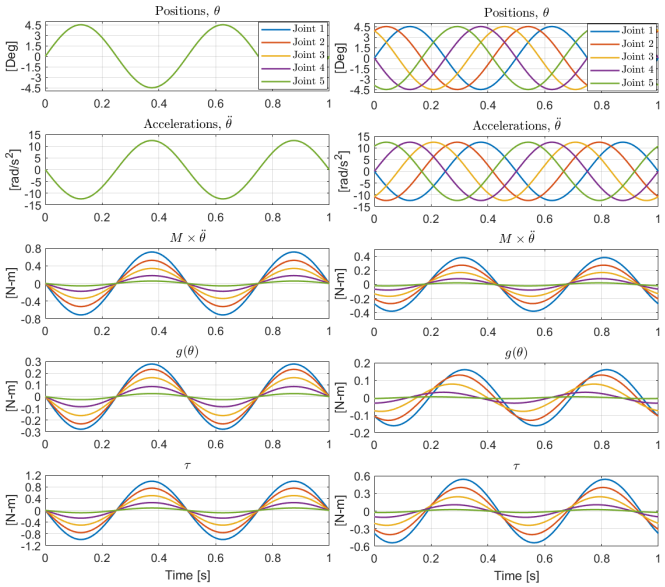

(a) (b)

Fig. 4: Spine dynamics with 4.5 deg amplitude at 2 Hz. Position changes from its zero configuration ($\theta = [\frac{\pi}{2},\ 0,\ 0,\ 0,\ 0]^T$) are shown: (a) Sinusoidal in-phase swing motion (b) $\pi/3$ phase-shifted motion.

torque decreases as the module number increases. For the phase-shifted motion shown in Fig. 4(b), each joint position reference is phase-shifted by $\pi/3$. Although acceleration $\ddot{\theta}$ is also phase-shifted, the $M\ddot{\theta}$ term is barely phase-shifted between modules, because mass matrix M elements for Joint 1 dominates the weight of the mass matrix. The peak of the gravitational torque $g(\theta)$ for the phase-shifted motion is lower than the one for the swing motion since the joint positions are not in phase. Overall the peak torque requirement for the swing motion is greater than the one for phase-shifted motion with greater $M\ddot{\theta}$ and $g(\theta)$ terms. The electromechanical spine simulation results are compared with the spine dynamics in Section III.

C. Torque, Current, and Position Relationship

Torque capability of the electromechanical actuator depends on its angular position and coil current. The torque is proportional to current squared when the core is not saturated [22]. Figure 5 presents the actuator's torque capability that varies with position and current. The results are from finite-element analysis using ANSYS Maxwell. The magnitude of torque is shown for Coil 1 excitation only. The actuator can produce significant amount of torque with high current. However, it becomes highly nonlinear due to core saturation when the current is high, especially when the joint position is fully rotated to the 4.5 deg position. Core saturation depending on current and position was discussed in [15]. Core saturation starts occurring above 3 A current and 1.5 Nm torque. Hence, the non-saturated region needs to be used to generate accurate torque from coil current. The torque

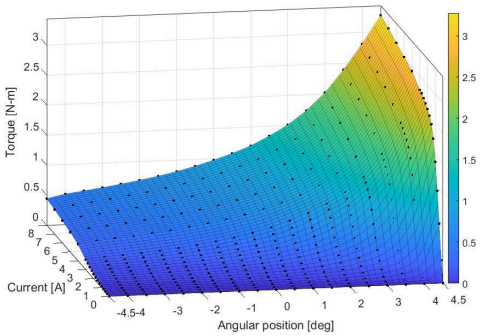

Fig. 5: Torque capability of the actuator depends on coil current and position.

curve when the coil current is at 1 A is selected to calculate the reference current for a reference torque at a position. Thus, the current can be expressed as

$$\tau_{ref} = \tau(\theta, 1A) \times i_{ref}^2,$$
$$i_{ref} = \sqrt{\frac{\tau_{ref}}{\tau(\theta, 1A)}}. \tag{6}$$

The torque curve at 1A shown in Fig. 5 and (6) are used in Section IV for torque-to-current conversion.

D. Position Control of the Spine

Position control of the spine with gravity and spring compensations in a vertical plane is developed. Both gravitational torque expressed in (5) and spring torque are compensated for a joint torque:

$$\tau = K_p\theta_e + K_d\dot{\theta}_e + g(\theta) + K\theta, \tag{7}$$

where K_p is proportional gain, K_d is derivative gain, K is spring rate at a joint, and θ is in degrees. A look-up table with linear-interpolation is used to compute a current reference from a torque reference for a specific position. The developed control framework for a module is shown in Fig. 6. Coil excitation is chosen based on the torque direction. A PI controller is used for individual coil current control. Coil current is limited to 3 A in order to operate in the non-saturated region in the full angular range. Torque is also limited to 1.5 Nm for the same reason.

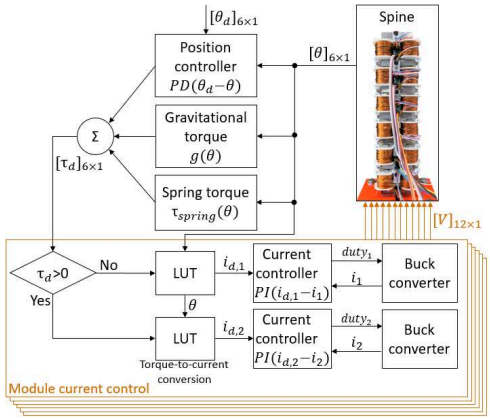

Fig. 6: Control framework of the spine.

E. Selection of Distributed Springs

Figure 7(a) shows the non-linear torque capability of the actuator, which reduces considerably for large airgaps. Reference [16] proposed a parallel spring mechanism to be used in conjunction with the actuator to reduce limitation. The spring mechanism consists of a combination of linear extension springs, which are attached to the upper and lower modules' coil holders, as shown in Fig. 8. The coil holder has three spring slots with a steel pin mount and up to three linear springs can be installed. The springs are pre-loaded. From a modeling perspective, the linear springs on both sides can be considered an equivalent torsional spring at the joint. Figure 7(b) shows the improvement in the torque capability by 5X for the maximum airgap position while sacrificing the torque by 25 % at the minimum airgap position with a spring rate of 0.1538 Nm/deg.

In vertical spine operation, the lower joints have a longer moment arm, which leads to a higher torque requirement. Depending on the module position, these variations in the actuator torque capability require different spring designs. The peak gravitational torque at the corresponding joint determines the lower bound of a module's spring rate. This constraint maintains the vertical position as equilibrium without an electrical torque. The upper bound of the module's spring rate is driven by the maximum torque requirement for a desired trajectory and acceleration. Various spring rates are chosen to counteract the gravity effect and meet the torque requirements, as listed in Table I. Springs are not used at Joint 6, since it requires small torque to move an I-shaped core. The torque capability of the actuator with the distributed springs is shown in Fig. 9.

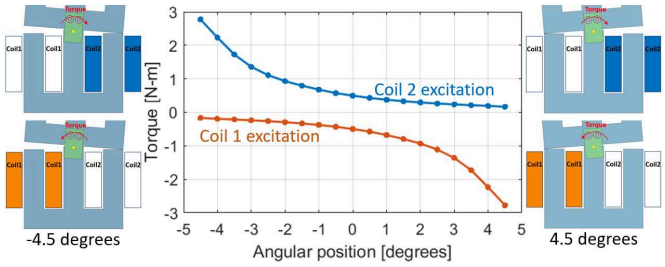

(a)

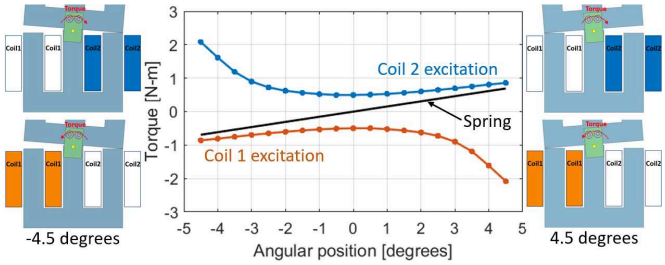

(b)

Fig. 7: Torque capability of the actuator at 3 A coil current: (a) Without springs (b) With spring rate of 0.1538 Nm/deg.

TABLE I: Combinations of different linear springs are used on the coil holders to create equivalent torsion spring rates.

Joint	1	2	3	4	5	6
# of spring 1 14.2 [lbs/in]	1	1	0	0	0	0
# of spring 2 4.69 [lbs/in]	2	1	3	2	1	0
Equivalent torsion spring [Nm/deg]	0.1538	0.1232	0.0927	0.0612	0.0306	0

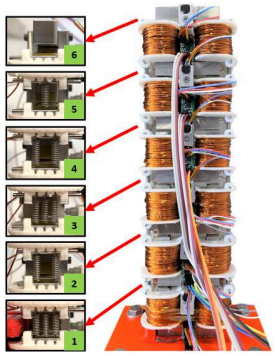

Fig. 8: Different combination of springs is used on each module.

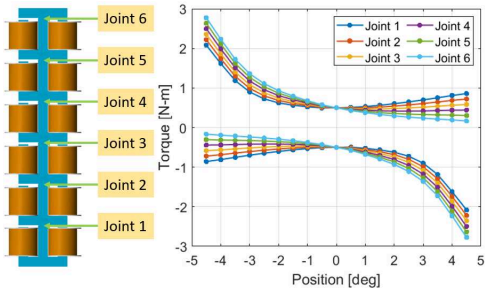

Fig. 9: Torque capability of the actuator at different joints for 3 A current with distributed springs.

III. Simulations

Matlab Simscape Multibody is used to compare the torque requirements between the analytical model and simulation. Right and left full swing motion and phase-shifted motion are simulated. The series-connected six modules, including the top I-shaped core, are set up in the simulation. The bottom module is fixed to ground. Joints 1-6 are located from the bottom to the top link in order. The spine is in a vertical plane.

Figure 10(a) and (b) compare the joint torques from simulation with the one from the spine dynamics model in Section II-B. The torque from the model at each joint matches well with simulation results for both swing and $\pi/3$ phase-shifted motions. The torque magnitude from the spine dynamics is marginally lower than simulation. The error is caused because the analytical model neglects the top I-shaped core and assumes point mass for each module in gravitational torque for model simplicity. The mass matrix is also considered to be a constant matrix due to the small angle changes at joints. For the swing motion, all joint torques are in phase, so Fig. 10(a) has a linear shape for all joints.

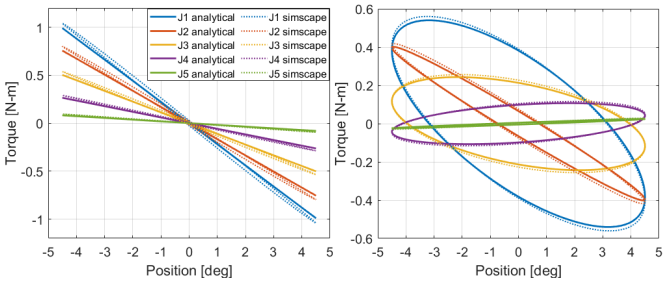

(a) (b)

Fig. 10: Torque versus position for 4.5 deg amplitude at 2 Hz: (a) Swing motion (b) $\pi/3$ phase-shifted motion.

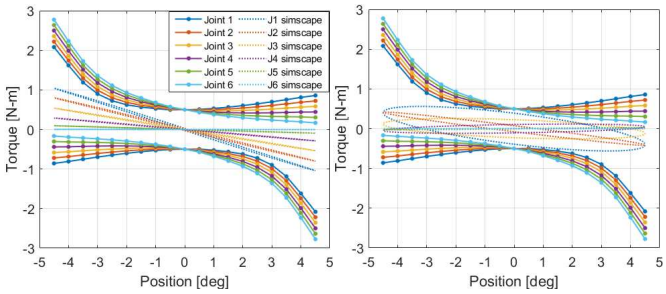

(a) (b)

Fig. 11: The required torque for the swing and phse-shifted motions are within the torque capability of the actuator with springs: (a) Swing motion (b) $\pi/3$ phase-shifted motion.

Joint 1 has the highest torque requirement because it has the longest moment arm. The torque curve for the phase-shifted motion in Fig. 10(b) presents tilted ellipses due to the phase-shifted torques, as shown in Fig. 4(b). The phase-shifted motion requires lower peak torques at –4.5 deg and higher peak torques around 0 deg than the swing motion. The higher torque requirements around 0 deg for the phase-shifted motion need higher coil currents due to the torque, position, and current relationship, as discussed in II-C.

These torque curves must stay within the actuator's torque capability to achieve the swing and phase-shifted motions. Figure 11(a) and (b) show that the torques are under the actuator's capability with its distributed springs.

IV. Experiments

Figure 12 shows the experimental setup for the spine's trajectory control. Figure 13 shows the system diagram. Six modules are stacked and connected to form the electromechanical spine in a vertical plane. The dimensions of the spine are $0.07(L) \times 0.03(W) \times 0.262(H)$ m^3, and the total weight is 1.9 kg. The lowest module is fixed to ground. The main 48 V power supply and auxiliary power supplies are connected to the power electronics. Both power electronics and the microcontroller (Texas Instruments F28379D) are located under the spine. The coils and position sensor outputs are connected to the power electronics board and controller. The computer communicates with the microcontroller to command and monitor joint positions and coil currents. The

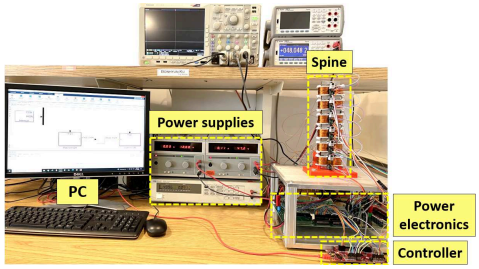

Fig. 12: Experimental setup for the spine controls.

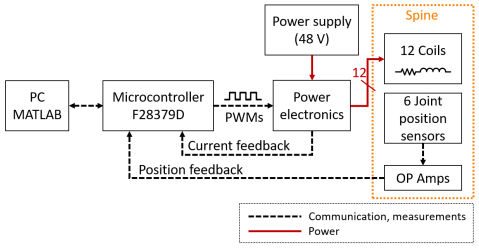

Fig. 13: System diagram of the electromechanical spine.

converter design is modular, so a total of twelve identical buck converters are mounted on the power electronics board.

A magnetic encoder is attached at the pin on the front side of the actuator to sense the position at each joint. The sensor is placed above the revolute joint pin while it does not touch the pin. A permanent magnet with a 3D-printed magnet holder is attached at the joint providing reference magnetic flux to the sensor. The position sensor outputs the position information as a sinusoidal waveform. The magnet is precisely located to utilize the linear region of the sinusoidal waveform at zero-crossing point, since the angular rotation is small. An operational amplifier circuit is used to amplify the position sensor output signal. The amplifier circuit is mounted on each module.

Figure 14(a) and 14(b) show the captured moments during the spine's swing motion with a 3 deg amplitude sinusoidal position reference at 1 Hz. Notice that the position changes from the spine's zero configuration are shown. The measured joint positions are shown in Fig. 15(a). All joint positions are in phase for the swing motion, and reach 3 deg. The swing

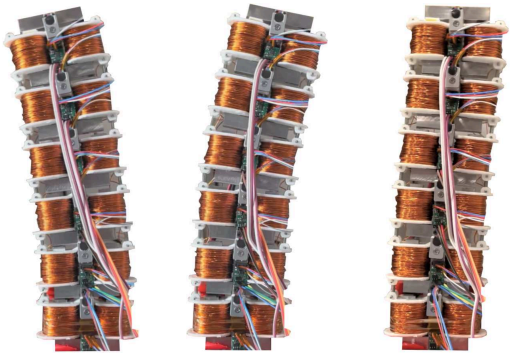

(a) Left (b) Right (c) Phase-shifted

Fig. 14: Swing and phase-shifted motions captured during vertical operation of the spine.

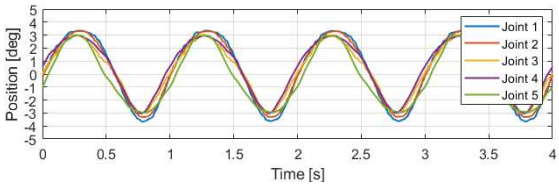

(a) Swing motion

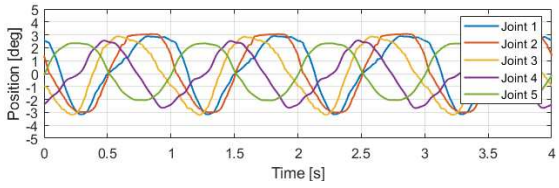

(b) $\pi/3$ phase-shifted motion

Fig. 15: Measured joint positions during undulatory motions with 3deg amplitude at 1 Hz.

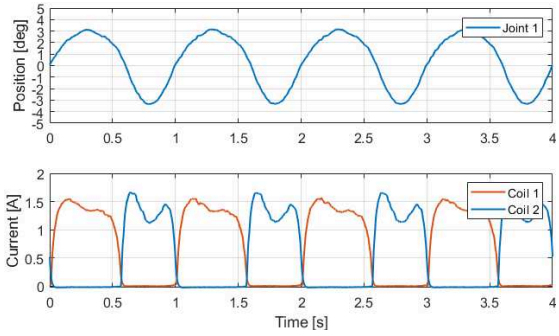

Fig. 16: Measured coil currents for module 1 during swing motion with 3 deg amplitude at 1 Hz.

motion makes 18 deg bending angle for the spine. Module 6 is not operated, since Joint 6 is fixed to 0 deg position. Measured positions of $\pi/3$ phase-shifted motion with the amplitude of 3 deg at 1 Hz is shown in Fig. 15(b). A captured moment during phase-shifted motion is shown in Fig. 14(c).

Coil currents are also measured for the same swing motion for Module 1 (Joint 1), as shown in Fig. 16. Since each coil creates opposing torque, the excitation is alternative for the sinusoidal waveform position reference. The actuator's torque capability at high angle is significantly higher than the one at low angle for same current, as shown in Fig. 5. Therefore, the coil current level decreases around 3 deg although its producing torque increases. The average input power for the swing and phase-shifted motions are 10 W and 15 W, respectively.

V. Conclusion

In this paper, position control of the distributed spine is developed. The spine dynamics is introduced as an open chain and approximated with its limited rotation. Gravitational and spring torques using measured positions are compensated. Distributed springs are installed on the spine to counteract gravity. In addition, electrical dynamics in the non-linear region is utilized to convert torque into current with position information. The controller is validated by the experimental results on the electromechanical spine in a vertical plane.

Acknowledgment

This material is based upon work supported by the National Science Foundation under Grant No. 1943791. The authors would also like to thank 3M Foundation and Power Affiliates Program at the University of Illinois Urbana-Champaign for supporting this work.

References

[1] I. Mizuuchi *et al.*, "The development and control of a flexible-spine for a human-form robot," *Advanced Robotics*, vol. 17, no. 2, pp. 179–196, 2003.

[2] N. Gravish and G. V. Lauder, "Robotics-inspired biology," *Journal of Experimental Biology*, vol. 221, no. 7, pp. 1-8, 2018.

[3] Y. Asano *et al.*, "Spine balancing strategy using muscle ZMP on musculoskeletal humanoid Kenshiro," *Robotics Research, Springer Proceedings in Advanced Robotics*, vol. 2, Springer, Cham, 2018.

[4] A. LaViers, "Make robot motions natural," *Nature*, vol. 565, pp. 422-424, 2019.

[5] O. Borisova *et al.*, "Design of galloping robots with elastic spine: tracking relations between dynamic model parameters based on motion analysis of a real cheetah," *IEEE/RSJ Int. Conf. on Intelligent Robots and Systems (IROS)*, pp. 8450-8455, 2021.

[6] S. Gracovetsky, "An hypothesis for the role of the spine in human locomotion: a challenge to current thinking," *Journal of Biomedical Engineering*, vol. 7, no. 3, pp. 205-216, 1985.

[7] S. Seok *et al.*, "Design Principles for Energy-Efficient Legged Locomotion and Implementation on the MIT Cheetah Robot," *IEEE/ASME Transactions on Mechatronics*, vol. 20, no. 3, pp. 1117-1129, 2015.

[8] M. Osada *et al.*,"Design of humanoid body trunk with "multiple spine structure" and "planar-muscle-driven" system for achievement of humanlike powerful and lithe motion," *IEEE Int. Conf. on Robotics and Biomimetics*, pp. 2217-2222, 2011.

[9] Y. Nakanishi *et al.*, "Design concept of detail musculoskeletal humanoid "Kenshiro" - Toward a real human body musculoskeletal simulator," *IEEE-RAS Int. Conf. on Humanoid Robots*, pp. 1-6, 2012.

[10] Y. Asano *et al.*, "Human mimetic musculoskeletal humanoid Kengoro toward real world physically interactive actions," *IEEE-RAS Int. Conf. on Humanoid Robots*, pp. 876-883, 2016.

[11] L. Roos *et al.*, "Design of a biomimetic spine for the humanoid robot Robota," *IEEE/RAS-EMBS Int. Conf. on Biomedical Robotics and Biomechatronics (BioRob)*, pp. 329-334, 2006.

[12] P. Rao *et al.*, "How to model tendon-driven continuum robots and benchmark modelling performance," *Frontiers in Robotics and AI*, vol. 7, 2021.

[13] M. Kawamura *et al.*, "A joint-space controller based on redundant muscle tension for multiple DOF joints in musculoskeletal humanoids," *IEEE-RAS 16th Int. Conf. on Humanoid Robots*, pp. 814-819, 2016.

[14] C. Cibert and V. Hugel, "Compliant intervertebral mechanism for humanoid backbone: Kinematic modeling and optimization," *Mechanism and Machine Theory*, vol. 66, pp. 32-55, 2013.

[15] B. Ku *et al.*, "Distributed and scalable electromechanical actuator for bio-inspired robots," *IEEE Int. Electric Machines and Drives Conf. (IEMDC)*, pp. 2180-2187, 2019.

[16] B. Ku *et al.*, "A spring-aided two-dimensional electromechanical spine architecture for bio-inspired robots," *IEEE/RSJ Int. Conf. on Intelligent Robots and Systems (IROS)*, pp. 793-798, 2019.

[17] B. Ku and A. Banerjee, "System-level design methodology for a distributed electromechanical actuator in bio-inspired robots," *IEEE Int. Electric Machines and Drives Conf. (IEMDC)*, pp. 1-8, 2021.

[18] R. Krishnan, *Switched Reluctance Motor Drives: Modeling, Simulation, Analysis, Design, and Applications*, CRC Press, 2001.

[19] R. Kelly, "PD Control with Desired Gravity Compensation of Robotic Manipulators: A Review." *The International Journal of Robotics Research*, vol. 16, no. 5, pp. 660–672, 1997.

[20] A. D. Luca, B. Siciliano, and L. Zollo, "PD control with on-line gravity compensation for robots with elastic joints: Theory and experiments," *Automatica*, vol. 41, no. 10, pp. 1809-1819, 2005.

[21] K. M. Lynch and F. C. Park, *Modern robotics - Mechanics, planning, and control*, Cambridge University Press, 2017.

[22] N. L. Schmitz and D. W. Novotny, *Introductory Electromechanics*, Ronald Press, 1965.